Applied Materials Today 37 (2024) 102116

Contents lists available at ScienceDirect

Applied Materials Today

journal homepage: www.elsevier.com/locate/apmt

Energy density enhancement of scalable thermoelectric devices using a low thermal budget method with film thickness variation

Jiyuan Huang [a], Rohan B. Ambade [b,c], Jacob Lombardo [a], Ben Brooks [a], Aswani Poosapati [a], Priyanshu Banerjee [a], Mortaza Saeidi-Javash [d], Yanliang Zhang [e], Deepa Madan [a,*]

[a] Department of Mechanical Engineering, University of Maryland Baltimore County, Baltimore, MD 21250, United States
[b] Advanced Research & Innovation Center, Aerospace Engineering, Khalifa University of Science & Technology, Abu Dhabi 127788, United Arab Emirates
[c] Department of Aerospace Engineering, Khalifa University of Science & Technology, Abu Dhabi 127788, United Arab Emirates
[d] Department of Mechanical and Aerospace Engineering, California State University Long Beach, Long Beach, CA 90840, United States
[e] Department of Aerospace and Mechanical Engineering, University of Notre Dame, Notre Dame, IN 46556, United States

ARTICLE INFO

Keywords:
p-type $Bi_{0.5}Sb_{1.5}Te_3$
n-type $Bi_2Te_{2.7}Se_{0.3}$
Composite thermoelectric films
Printed thermoelectric device
LED light up
Capacitor charging

ABSTRACT

Additive manufacturing has been investigated as a more time, energy, and cost-efficient method for fabricating thermoelectric generators (TEGs) compared to traditional manufacturing techniques. Early results have been promising but are held back by including a high-temperature, long-duration curing process to produce high-performance thermoelectric (TE) films. This work investigates the synergistic effect of four factors – a small amount of chitosan binder (0.05wt%), a combination of micron and nano-sized particles, the application of mechanical pressure (20 MPa), and thickness variation (170, 240, 300 μm) – on the performance of stencil printed p-$Bi_{0.5}Sb_{1.5}Te_3$ (p-BST) and n-$Bi_2Te_{2.7}Se_{0.3}$ (n-BTS) TE composite films. The combination of these four factors controls the micro and nanostructure of the films to decouple their electrical and thermal conductivity effectively. This resulted in figures of merit (ZTs) of 0.89 and 0.5 for p-BST and n-BTS thinner (170 μm) films, respectively, comparable to other additive manufacturing methods despite eliminating the high-temperature, long-duration curing process. The process was also used to fabricate a 6-couple TEG device, which could generate 357.6 μW with a power density of 5.0 mW/cm^2 at a ΔT of 40 K. The device demonstrated air stability and flexibility for 1000 cycles of bending. Finally, the device was integrated with a voltage step-up converter to power an LED and charge and discharge capacitor at a ΔT of 17 K, demonstrating its applicability as a self-sufficient power source.

1. Introduction

Thermoelectric generators (TEGs) directly convert waste heat into valuable electrical energy and have been proven to be one of the most promising energy harvesting devices because of their reliability, scalability, relatively small volume, and adaptability to various environments [1–3]. Flexible TEGs (*f*-TEGs) fabricated using additive manufacturing methods such as direct printing, inkjet printing, or screen printing innovate on traditional devices due to their advantages in cost, scalability, and manufacturing efficiency. Moreover, these *f*-TEGs can scavenge waste heat from non-planar surfaces (e.g., human body) and potentially be used as a self-sufficient power source for various applications such as flexible electronics, health monitoring sensors, and wearable devices. Therefore, a process for fabricating high-performance *f*-TEGs using additive manufacturing is desirable [4–11]. Printing thermoelectric (TE) films with a high figure of merit (ZT) is essential to fabricate high-performance *f*-TEGs, as it can directly reflect the TEG's power output and power density. In the past, the printed TE films had a relatively lower ZT than bulk materials due to the high weight ratio of the insulating binder and the poor interfacial connections between the TE particles and the polymer binder [12–14]. As a result, many efforts have been devoted to improving the ZT value of printed TE composites, including using long, high-temperature sintering processes, removable binders, adding Se and Te additives, densification via mechanical pressure, and post-processing techniques [15–21]. These new techniques have significantly improved the ZT of printed TE films, with the best-reported films reaching ZTs of 1.0 for p-BST and 0.6 for n-BTS [17–21]. However, each new step of the manufacturing process

* Corresponding author.
E-mail address: deemadan@umbc.edu (D. Madan).

https://doi.org/10.1016/j.apmt.2024.102116
Received 21 November 2023; Received in revised form 25 January 2024; Accepted 4 February 2024

introduced to improve the films' performance has also increased the time and energy required to produce them. In particular, the high-temperature, long-duration (~500°C for up to 18 h) sintering process negated the time and energy advantage of additive manufacturing over traditional manufacturing methods [16–20]. More information and comparison of the high energy consumption and long duration between different methods and literatures are shown in **Table S1** in the supplemental file.

Existing literature demonstrated the film thickness dependence only for thin films (hundreds of nanometers or several micrometers) [22–24]. Han *et al.* used chemical vapor deposition (CVD) to fabricate p-type Sb_2Te_3 thin films at a thickness range of 1-16 μm and achieved a maximum electrical conductivity of 666 S/cm at the lowest thickness (1 μm) [23]. Wang *et al.* used electron-beam evaporation to fabricate p-type Sb_2Te_3 thin films with thicknesses between 10 to 100 nm. A maximum electrical conductivity of 700 S/cm was also achieved at the lowest thickness (10 nm) with decreases in defects and interfaces [22]. Physical techniques like CVD and physical vapor deposition (PVD) are costly and time-consuming. They grow films by repeatedly depositing thin layers, which could introduce extra defects, interparticle interfaces, and void formations. As an alternative, in this work, we have used a cost-effective and energy-efficient additive manufacturing technique to print thermoelectric films and TEGs with thicknesses in the range of hundreds of microns. However, the thickness effect in printed composite films (up to 300 μm) has not been systematically studied. This work aims to systematically investigate the effect of thickness together for next-generation *f*-TEGs with optimized performances fabricated *via* energy-efficient and scalable manufacturing processes.

Our previous works reported a low-energy-input printing method for fabricating n-BTS and p-BST composite films and single-leg devices using the synergistic effects of (1) a small amount of chitosan binder (0.05 wt%), (2) heterogeneous (mixed nanoscale and microscale) TE particles, and (3) applied mechanical pressure of 20 MPa combined with curing at a low temperature of 120°C for 30 mins [25–29]. **Table S2** and **S3** (Supporting Information) compare this current research work with our previously reported printed TE composite work. While the results of these experiments were promising, the performance of films produced by our low-energy input process was lower than those produced by the energy-intensive sintering process. Therefore, we hypothesize that the reduction in film thickness, similar to what was observed in previously researched thinner films (1-16μm) produced through vapor deposition, will lead to a reduction in the occurrence of defects increasing electrical conductivity in our 170 μm films when compared to our 300 μm films. More generally, defect concentration and nature within TE films seem critical in optimizing film performance. With this in mind, we introduced a fourth synergistic factor – thickness variation – to our process, intending to produce films with micro and nanostructures that optimized electrical conductivity while simultaneously reducing thermal conductivity, effectively decoupling the two properties. Finding high-performance n and p-type films will allow high-energy density *f*-TEG devices to be manufactured at scale without expending much time or energy.

Each of the four synergetic factors influences the micro and nanostructure and interfaces of the films differently. We assume that tuning the weight ratio of the naturally occurring and low-cost Chitosan binder will produce composite microstructures that will not affect the electrical connection among active TE particles while facilitating interfacial thermal resistance among particles and the polymer micron-sized particles that provide a large mean free path for charge carriers and nano-sized particles and interfacial defects facilitating phonon scattering. Additionally, tuning external uniaxial pressure will initiate lattice defects, resulting in high-weighted mobility and phonon vibrations. We hypothesize that a film with a lower thickness (~170 μm compared to 300 μm) will have fewer micron-scale defects (grains, grain boundaries, and interfaces), resulting in less charge carrier scattering and high electrical conductivity. Moreover, we assume different film thicknesses will experience the effect of other synergetic factors differently. An important aspect of the proposed low-thermal budget additive-manufacturing method is that it promises to eliminate the need for the current state-of-the-art long-duration and high-temperature curing process, decouple electrical and thermal conductivity, and achieve high-performance composite TE films. This results in a process whose only energy-consuming component is the application of mechanical pressure, which had previously been used together with the high-temperature curing process [23,24,30].

Thus, this work demonstrated the fabrication of n and p-type free-standing films using this low-thermal budget approach to overcome the issues of the high-temperature curing process to allow for widespread adoption of TEGs as illustrated in Fig. 1. The effect of thickness on thermoelectric parameters was explored. Air stability and flexibility tests showed the real-world durability of our TEG manufacturing technique. Finally, the *f*-TEG device's capability as a self-sufficient power source was demonstrated by integrating it with a step-up circuit to light a blue LED and charge a capacitor. Fig. 1 illustrates the importance of all synergistic factors to produce scalable *f*-TEGs with high energy density.

The free-standing films achieved high electrical conductivity for both chitosan p-BST-100 mesh (660 S/cm) and chitosan n-BTS-100 mesh (286 S/cm) films of 170 μm owing to the smaller number of micro-scale defects (pores, interfaces, grain boundaries) compared to 240 μm and 300 μm films. The nano-sized defects, particles, pores, and interfaces resulted in a low thermal conductivity of 0.77 W/m-K for p-BST and 0.65 W/m-K for n-BTS films. We decouple electrical and thermal conductivity using interfacial engineering and a low-thermal budget additive manufacturing approach. High electrical conductivity and low thermal conductivity resulted in a high ZT of 0.89 for p-BST and 0.50 for n-BTS composite films, which is 25% higher than our previously reported ZT for p and n composites [25–27]. Further, a 6-couple flexible device was stencil printed using p-BST and n-BTS composite inks. A maximum open circuit voltage of 91 mV and a maximum power output of 357 μW was achieved at a temperature difference (ΔT) of 40 K. The device exhibited a power density of 5.0 mW/cm^2, a 40% improvement from our previously best-reported TEG devices [17-21,25-27,30]. A flexibility test was performed by bending the TEG device at a 3-cm radius for 1000 cycles. Electrical resistance was chosen to evaluate the flexibility of the TEG device due to its sensitivity to cracking with bending [18]. The TEG device experienced only 4.3% increase in internal resistance and no measurable change in voltage at a ΔT of 40 K, as seen in **Fig. S16**. An air stability test was conducted by exposing the TEG device to ambient air for more than six months, showing an increased resistance of 23% and no measurable change in voltage at a ΔT of 40 K. Finally, the TEG device capability as a self-sufficient power source in a real-world application was demonstrated by lighting a blue LED and charging a capacitor at a ΔT of 17 K when integrated with a step-up circuit. These demonstrations proved the potential application of printed *f*-TEGs as a self-sufficient power supply for wireless sensor devices to monitor physical parameters continuously.

2. Experimental Section

2.1. Materials

The materials used in the research, 100 mesh $Bi_{0.5}Sb_{1.5}Te_3$ (BST-100) and $Bi_2Te_{2.7}Se_{0.3}$ (BTS-100) were purchased from Wuhan Dongxin Inc., China. The 100 mesh TE particles contain a mixed distribution of micron and nano-sized TE particles [25]. Chitosan powder (MP Biomedicals, LLC), Dimethyl sulfoxide (DMSO, ≥99.7%, extra dry, ACROS Organics), and Salicylic acid were purchased from Fisher Scientific. The 5 mm thick non-adhesive Kapton substrate was purchased from Caplinq, Canada, and used as masking tape.

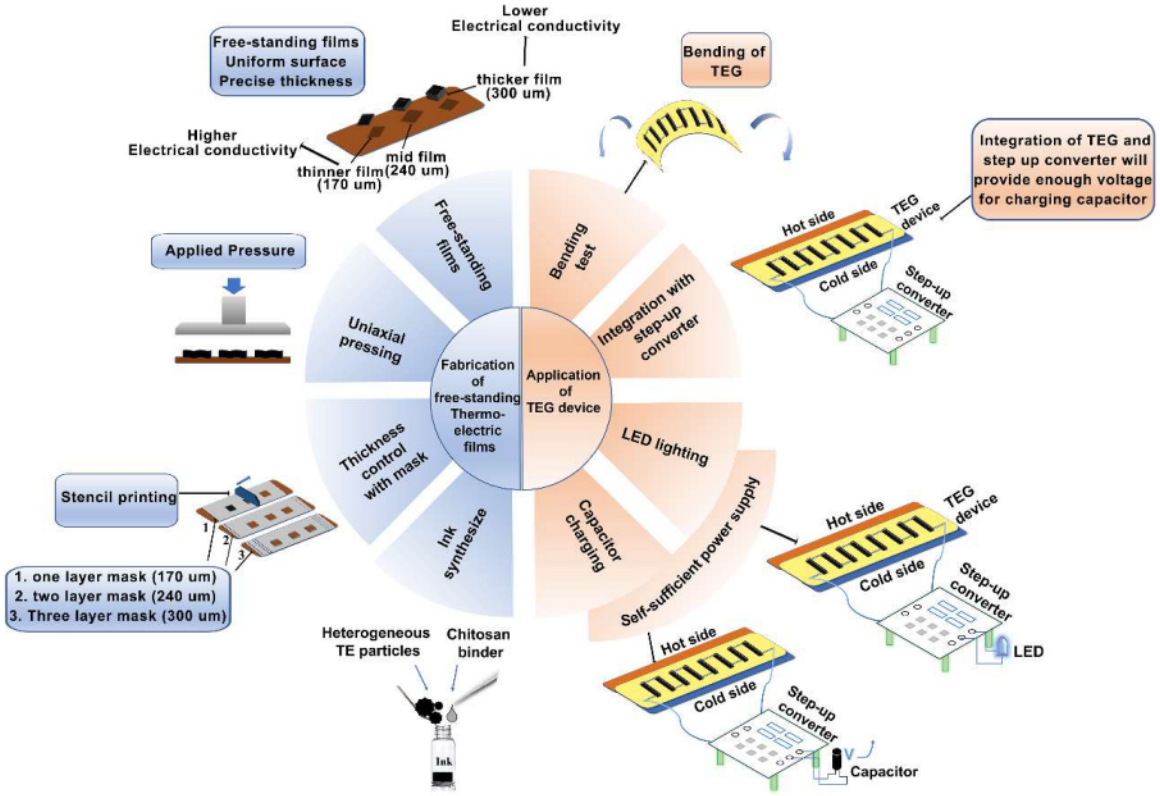

Fig. 1. Graphical research flow for fabricating high-performance n and p free-standing films by investigating the impact of low binder concentration, heterogeneous particle size distribution, mechanical pressure, and thickness to produce scalable and high-energy density *f*-TEG devices.

2.2. Ink preparation

The Chitosan binder solution was synthesized by mixing DMSO, Salicylic acid, and Chitosan powder and stirring at 60°C for 24 h. The inks (BST and BTS separately) were synthesized by mixing Chitosan binder and active TE particles at a weight ratio of 1:2000 [25,27]. Inks were mixed in a vortex mixer for 2 mins and in an ultrasonic mixer for 30 mins.

2.3. Free-standing film fabrication

Free-standing BST and BTS composite films were prepared to ensure the accuracy of film thicknesses. Free-standing films eliminate the error of thickness measurements caused by non-planar Kevlar substrate [25–27]. Multiple layers of the mask were stacked together to control the thickness of the film. A custom-designed printing mask was prepared by stacking several layers (1, 2, and 3) of single-side tape (*Business Source*®), resulting in 170, 240, and 300 μm film thicknesses. The film fabrication with a lower thickness was not applicable due to the limitation of the minimum thickness of a single-layer mask (170 μm). Using a CNC laser cutter, a mask pattern was designed using Solidworks software and cut onto the mask tape. The mask was then attached to the Kapton substrate, and the TE ink was stencil printed. The printed films were cured at a low temperature of 120°C for 10 mins and then pressed at 20 MPa for 30 mins. Pressures above 20 MPa were tested to evaluate their effects on TE parameters, and no significant improvements were found, leading to the selection of 20 MPa for the applied pressure used in this work. The applied pressure was among the lowest compared to other works, as many used 100-200 MPa [18,19,29]. Due to Kapton's low adhesion, the films could then be transferred to a fresh substrate fitted with double-sided tape for a more accurate thickness measurement (**Fig. S1,** Supporting Information). Each film measured approximately 7 mm × 7 mm.

2.4. Device fabrication

The TEG device was fabricated on a flexible Kevlar substrate with a gold-coated Cu electrode. (Purchased from South Korea PASF250, Sueco Advanced Material Co., Ltd). Before printing, a commercially available solder paste was coated on the gold electrodes to improve the electrical and mechanical connections between TE elements and electrodes [29]. Then, p-type BST-100 and n-type BTS-100 composite inks were stencil printed in an alternating pattern on the substrate. The same type of single-layered mask (*Business Source*®) was used to help print the desired dimension of the thermoelements. The pattern on the mask was manufactured by a laser cutter with dimensions of (2 mm × 6 mm) (width × length) for each thermoelement. Then, the device was cured at 120°C for 10 mins and 20 MPa for 30 mins. Each thermoelement measured approximately 3 mm × 7 mm.

2.5. TE properties measurement and characterizations

The in-plane electrical conductivity, carrier concentration, and mobility measurements were measured in ambient conditions using the Hall Effect measurement system (ECOPIA, HMS-5500) [24–29]. The Seebeck Coefficient was measured using a custom-built system [25–29]. To measure the in-plane thermal conductivity of thick TE composite printed films (100-1500 μm), researchers have mainly used the Angstorm method and laser flash LFA 457 from Netzsch company (**Table S4** Supporting Information) [17-21,25,26]. The Angstrom method was selected to measure the thermal conductivity of our films, as detailed in **Table S4**, based on its demonstrated reliability in providing consistent results for similarly printed films. [18,25,54]. In addition, X-ray diffraction (XRD), scanning electron microscopy (SEM), high-resolution transmission electron microscopy (HRTEM), Brunauer–Emmett–Teller (BET), energy dispersive X-ray analysis (EDAX), and Raman Analysis were performed to show the composite microstructure, heterogeneous

particle size (micro-sized and nano-sized) distribution, interfaces among particles and chitosan, micro-/nano-sized defects in the cross-sectional area of the films, as well as pore number and volume within films. The detailed characterization information was shown in the Supporting Information.

3. Results and Discussions

3.1. XRD and Raman spectra analysis

Fig. 2**a** shows that the X-ray diffraction (XRD) patterns for p-BST powder, p-BST 170, and 300 μm thickness films are consistent with the standard database of the BST XRD peaks (JCPDS 49-1713) [31,32]. Chitosan peaks are not visible due to the very low concentration of chitosan within the films (0.05wt%). Fig. 2**b-d** shows the Raman spectra for p-BST powder, 170 and 300 μm thickness films. The Raman peaks A_{1g}^1, E_g, A_{1g}^2 at the phonon vibration modes exist at 62, 102, and 135 cm^{-1} for both p-BST 170 and 300 μm thickness films indicate the presence of BST (Fig. 2**c**). The peak for p-BST and n-BTS 170 and 300 μm thickness films at ~1470 cm^{-1} indicate the presence of chitosan (1400 cm^{-1}) (Fig. 2**d, h**) [33,34]. After including BST/BTS and applying uniaxial pressure in the composite films, a slight Raman peak shift was observed. The XRD pattern and Raman spectra show the presence of both chitosan and BST materials in p-BST composite 170 and 300 μm film thickness [25,33,34]. Similarly, the XRD and Raman spectra were investigated for n-BTS powder and n-BTS composite for 170 and 300 μm film thickness and chitosan powder. The XRD peaks (Fig. 2**e**) are consistent with the standard database of the BTS XRD spectra (JCPDS 50-0954) [35]. Fig. 2**f-h** shows the Raman spectra of n-BTS powder, n-BTS 170, and 300 μm thickness films. The Raman peaks A_{1g}^1, E_g, A_{1g}^2 at the phonon vibration modes exist at 65, 118, and 139 cm^{-1} for both n-BTS 170 and 300 μm thickness films indicate the presence of BTS (Fig. 2**g**) [33,36]. A Raman peak shift was observed for both p-BST and n-BTS composite films (Fig. 2**c, g**) due to applying pressure during fabrication, as explained in Section 3.4.

3.2. Electrical conductivity

Fig. 3 shows the electrical conductivity, Seebeck coefficient, carrier concentration, mobility, power factor, and density of p-type BST-100 and n-type BTS-100 composite films with respect to the film thicknesses (170, 240, and 300 μm). Fig. 3**a** shows an inversely proportional relationship between the electrical conductivity and thickness for p-BST and n-BTS composite films. The TE properties of the 240 μm n and p films lie between those of the 170 and 300 μm films, as illustrated in Fig. 3**a-e**. To simplify the comparison of TE properties with film thickness, we will focus on 170 and 300 μm films. The average electrical conductivity of 660 S/cm was achieved for p-BST 170 μm films and 555 S/cm for 300 μm films. The electrical conductivity increased by approximately 20% from 300 μm to 170 μm films. Similarly, the average electrical conductivity of 286 S/cm was achieved for n-BTS 170 μm films and 182 S/cm for 300 μm films, showing an about 54% increase in electrical conductivity. These results indicate that p-BST and n-BTS films have higher electrical conductivities at lower thicknesses.

3.3. Seebeck coefficient and Power factor

Fig. 3**b** shows the absolute Seebeck coefficient value of p-BST and n-BTS films with respect to their thickness. The average Seebeck coefficient of 186 μV/K and 194 μV/K was achieved for p-BST 170 and 300 μm films, respectively. The average absolute Seebeck coefficient for n-BTS 170 and 300 μm films was 194 μV/K and 203 μV/K, respectively. The Seebeck coefficients slightly increased for p-type and n-type films with increased film thicknesses. The result can be attributed to the slight decrease in carrier concentration. The carrier concentration of p-BST films decreased from 3.6×10^{19} (170 μm) to 3.2×10^{19} (300 μm), and the values of n-BTS films decreased from 170 μm 3.2×10^{19} (170 μm) to 2.4×10^{19} (300 μm) as shown in Fig. 3**c**. Therefore, the Seebeck Coefficients for both p and n-type films slightly increased from 170 μm to 300 μm (Fig. 3**b**) based on Eq. (1) [1].

$$S = \frac{8\pi^2\kappa_B^2}{3eh^2} m^* T \left(\frac{\pi}{3n}\right)^{2/3} \quad (1)$$

where n is the carrier concentration, κ_B is the Boltzmann constant, h is the Plank constant, and m^* is the effective mass of the carrier. Moreover, the absolute Seebeck coefficient of p-BST (186 μV/K - 194 μV/K) and n-BTS films (194 μV/K - 203 μV/K) were comparable to reported values of existing printed films, and bulk p-BST and n-BTS, respectively [17,19,20,25,27]. The mobility of p-BST 300 μm films (120 cm^2/V-s) was slightly lower than the mobility (125 cm^2/V-s) of 170 μm films (Fig. 3**d**). Moreover, a decrease in mobility from 62 cm^2/V-s for n-BTS 170 μm films to 55 cm^2/V-s for 300 μm films was also observed (Fig. 3**d**).

The average power factor for p-BST 170 and 300 μm films was 2300 and 2070 $\mu W/mK^2$, respectively, as shown in Fig. 3**e**. The BST films with a thickness of 170 μm had an 11% higher power factor than 300 μm films. The highest power factor for p-BST 170 μm films (2300 $\mu W/mK^2$) is comparable to other reported values of printed films in existing literature [17,19,20,25]. The power factor for p-BST was lower than bulk BST (5200 $\mu W/mK^2$) due to the decrease in electrical conductivity (Fig. 3**e**). The average power factor for n-BTS 170 and 300 μm thickness films were 1100 and 778 $\mu W/mK^2$, respectively. The BTS 170 μm films have 41% higher power factor than 300 μm films.

The highest power factor for n-BTS 170 μm films (1100 $\mu W/mK^2$) were lower than other reported values for printed films and bulk values, mainly due to the lower electrical conductivity and film oxidation [17,19,20,27]. These films were produced with a fraction of the time and energy investment required by other printing methods, making this a worthwhile tradeoff in many circumstances. Fig. 3**f** shows the density of p-BST and n-BTS 170 μm and 300 μm films. The average density achieved for p-BST films was 6.02 and 5.93 g/cm^3 for 170 and 300 μm thickness films, respectively. The highest density of p-BST 170 μm films (6.02 g/cm^3) was about 89% that of bulk p-BST [20,37]. This density value is amongst the highest reported values for printed TEG films [20,25]. The average density achieved for n-BTS films was 6.25 and 6.12 g/cm^3 for 170 and 300 μm thickness films, respectively. The highest density of n-BTS 300 μm films (6.25 g/cm^3) was about 86% of the bulk n-BTS density [38]. The value is among the highest reported values from other literature with printed films [20,27]. The comparable density between 170 and 300 μm thickness films for p-BST and n-BTS in this work indicates that the thickness variation has a minor effect on film density.

The highest electrical conductivity of p-BST films was improved by 9% from our previous work and is comparable to the best-reported electrical conductivity of printed films [17-20,25]. This can be attributed to the free-standing films with precise thickness measurements and the microstructure changes in 170 μm film [25]. However, the highest achieved electrical conductivity of p-BST 170 μm films (660 S/cm) was still lower than that of bulk p-BST (1100-1200 S/cm) [39]. This lower electrical conductivity can be attributed to the increased number of defects found within the 11% lower film density of p-BST films compared to bulk BST. On the other hand, the highest electrical conductivity (286 S/cm) of n-BTS 170 μm films was improved by 43% from our previous work and comparable with other printed films [17,19,20,27]. This increase in electrical conductivity compared to our previous work can be attributed to the lower charge carrier scattering found within thinner free-standing films with precise thickness measurements and a 3% increase in film density. This electrical conductivity of n-BTS composite is less than half of bulk n-BTS (800 S/cm) values due to the lower density of n-BTS at 86% that of bulk and the oxidation of n-BTS films in ambient air [40–42].

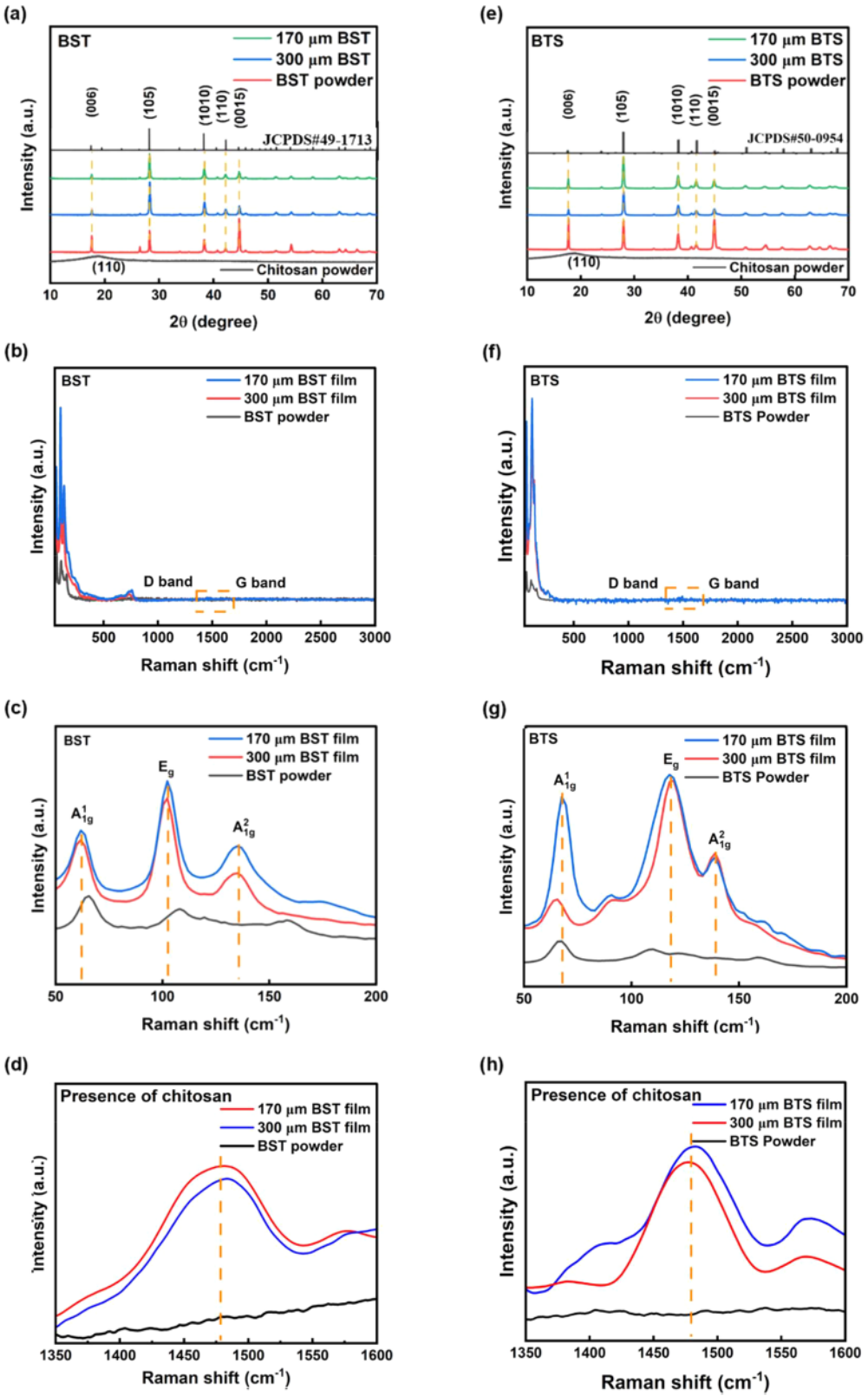

Fig. 2. (a) XRD patterns and (b) Raman spectra of BST powder, chitosan powder, BST-chitosan composite 170 and 300 μm thickness films, (c-d) Raman spectra of BST powder and BST-chitosan composite 170 and 300 μm thickness films showing the peaks of BST and the Chitosan peak in BST composite films, (e) XRD patterns and (f) Raman spectra for BTS powder, BTS-chitosan composite 170 and 300 μm thickness films, (g-h) Raman spectra of BTS powder and BTS-chitosan composite 170 and 300 μm thickness films showing the BTS peaks and Chitosan peak in and BTS composite films.

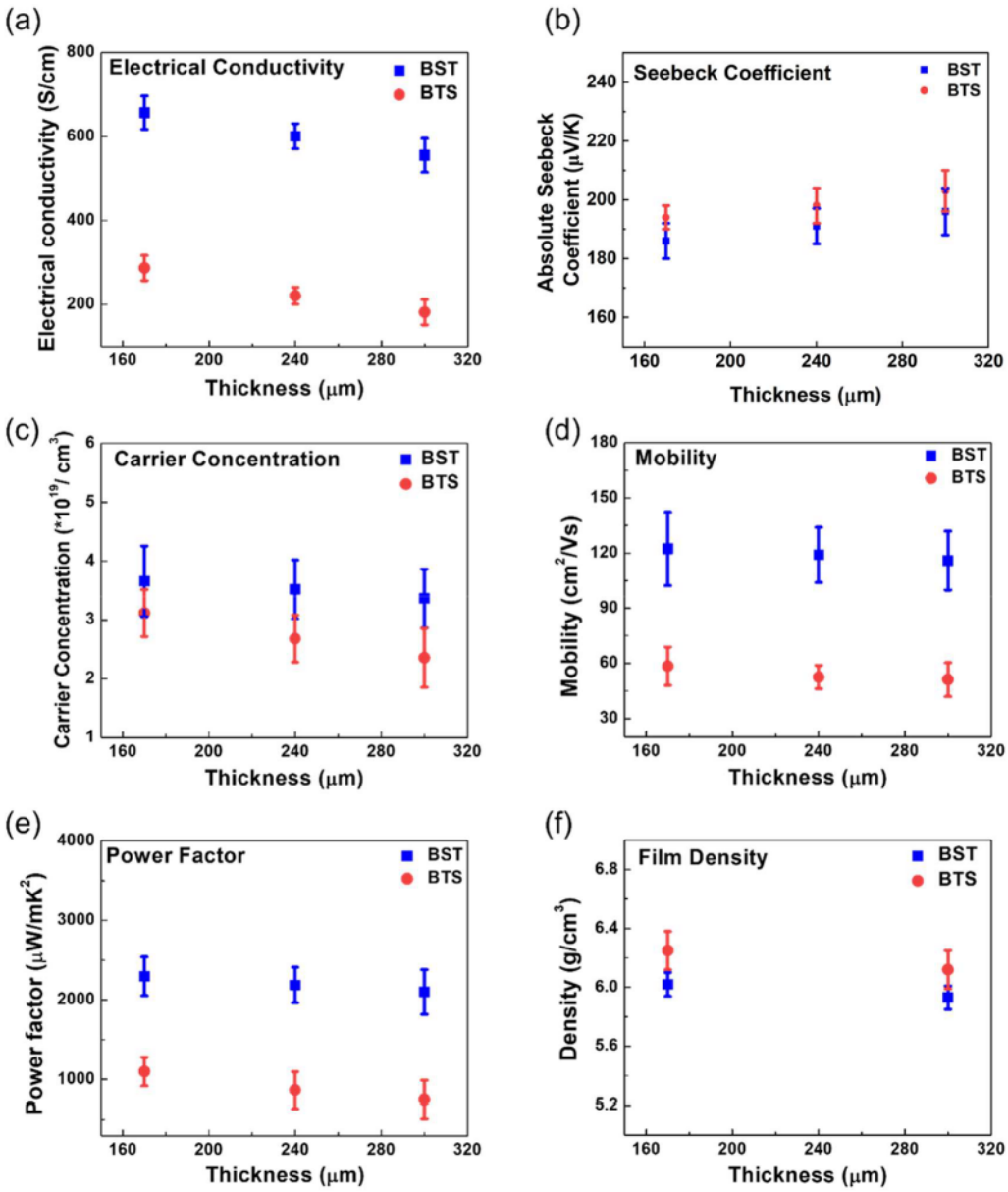

Fig. 3. (a) Electrical conductivity, (b) absolute Seebeck coefficient, (c) carrier concentration, (d) carrier mobility, (e) power factor, and (f) film density of BST-100-chitosan and BTS-100-chitosan composite films with respect to the thicknesses.

The effect of thickness and microstructure changes on electrical conductivity and mobility for 170 and 300 μm thickness p-BST and n-BTS composite films were investigated using scanning electron microscopy (SEM). The grain, grain boundaries, grain interfaces, and micro-sized defects within the films at different thicknesses were investigated using SEM images (Fig. 4). The cross-sectional 100μm SEM images of our thinner and thicker p-BST and n-BTS films (Fig. 4**b, d, f, h**) showed minor thickness variations compared to Vernier caliper measurements. The difference between SEM and Vernier caliper-measured thickness can be attributed to the fact that the Vernier caliper measures the thickness of the film between its jaws, whereas SEM measures film thickness in a small film region. The film thickness measured by SEM can be sensitive to the particle-size variations in the starting thermoelectric material. Given the particle size variation (particles up to 50 μm size) in the starting thermoelectric material, the SEM thickness measurements are within the expected range.

The results confirmed the thickness measurement accuracy and the difference between the 170 and 300 μm thickness films. Fig. 4**a, c, e, g** shows the grains, grain boundaries, particle interfaces, and pores of p-BST and n-BTS for the 170 and 300 μm thickness films, respectively. The top-view SEM image of the p-BST 300 μm thickness film shows more grains and pores (Fig. 4**a**) than the 170 μm thickness film (Fig. 4**c**).

ImageJ software was used for the SEM images (Fig. 4**b, d, f, h**) of p-BST and n-BTS 300 and 170 μm thickness films to acquire particle size and particle numbers, as shown in **Fig. S2**. The number of grains in p-BST 300 μm films is almost double that of p-BST 170 μm films (**Fig. S2a-b**). Similarly, the number of grains in n-BTS 300 μm films is nearly double that of n-BTS 170 μm films (**Fig. S2c, d**). This difference can be attributed to the thickness variation of the films. The 300 μm thickness films have a higher TE particle count when film area and particle size are fixed. The higher number of particles increases grains, grain boundaries, interfaces, and micro-sized defects in the composite films, forming a short mean free path, causing increased charged carrier scattering, and reducing the carrier concentration. Thus, reduced carrier mobility, carrier concentration, and electrical conductivity were obtained for p-type and n-type 300 μm thickness films [43,44]. On the contrary, 170 μm

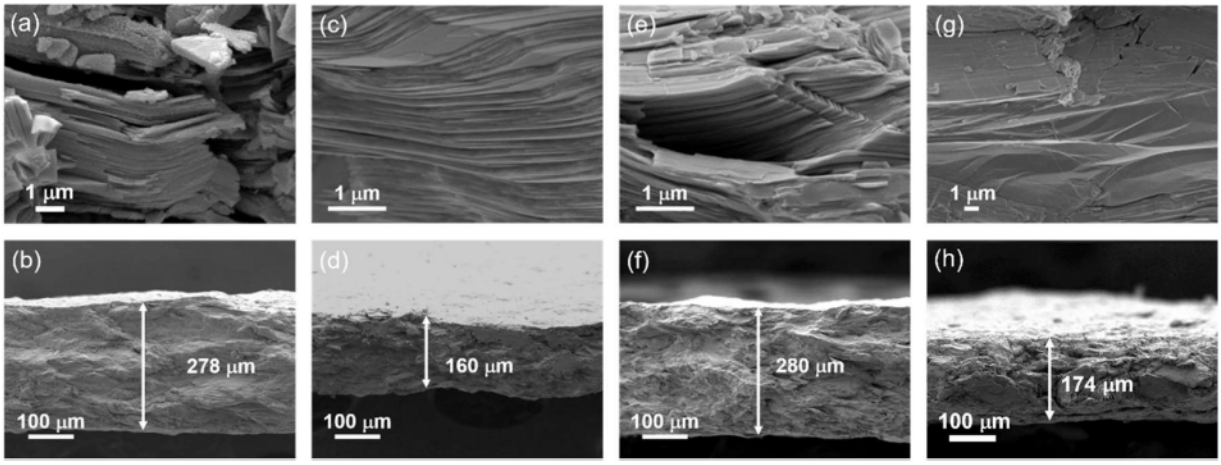

Fig. 4. SEM cross-section images (1 μm and 100 μm) of p-BST and n-BTS composite films with different thicknesses: (a-b) 300 μm BST, (c-d) 170 μm BST, (e-f) 300 μm BTS, and (g-h) 170 μm BTS.

thickness films have a smaller TE particle count, thus containing fewer grain boundaries and grains that can form a longer mean free path. Therefore, 170 μm thickness films exhibited less charged carrier scattering, higher mobility, and electrical conductivity [43–45].

3.4. Thermoelectric properties across an increase in temperature

Fig. 5 shows the TE properties (electrical conductivity, Seebeck coefficient, Power factor, and Weighted Mobility) of p-BST and n-BTS 170 μm films at increasing temperatures. The temperature-dependent measurements suitable for low waste heat applications were performed at 298, 323, 348, and 373 K [12,15,46]. Fig. 5**a** shows the electrical conductivity of both p-BST and n-BTS films at increasing temperatures. The electrical conductivity of p-BST films was 660 S/cm at 298 K and 600 S/cm at 373 K. The slight decrease in electrical conductivity with increased temperature indicates its semi-metallic behavior, consistent with previous reports [18,25,46]. Conversely, the electrical conductivity for n-BTS films was 286 S/cm at 298 K and 290 S/cm at 373 K. The slightly increasing trend in electrical conductivity with increased temperature indicates its semiconducting behavior [15]. The absolute Seebeck coefficient for p-BST and n-BTS films did not change significantly with an increase in the temperature (Fig. 5**b**). The power factor for p-BST 170 μm films decreased slightly due to the decrease in the electrical conductivity and a comparable Seebeck coefficient (Fig. 5**c**). The power factor for n-BTS films increased slightly due to increased electrical conductivity and a comparable Seebeck coefficient (Fig. 5**c**).

The average weighted mobility was calculated using Snyder's formula, Eq. (2), and measured electrical conductivity and the Seebeck coefficient of p-BST and n-BTS 170 μm films, respectively [47]:

$$\mu_w = 331\frac{cm^2}{Vs}\left(\frac{mW\ cm}{\rho}\right)\left(\frac{T}{300K}\right)^{-3/2}\left[\frac{\exp\left[\frac{|S|}{\frac{k_B}{e}}-2\right]}{1+\exp\left[-5\left(\frac{|S|}{\frac{k_B}{e}}-1\right)\right]}+\frac{\frac{3}{\pi^2}\frac{|S|}{\frac{k_B}{e}}}{1+\exp\left[5\left(\frac{|S|}{\frac{k_B}{e}}-1\right)\right]}\right] \quad (2)$$

where μ_w is the weighted mobility, ρ is the electrical resistivity, T is the absolute temperature, S is the Seebeck coefficient, and k_B/e is 86.3 μV/K. The average weighted mobility of p-BST 170 μm films was 272 cm^2/V-s at room temperature and decreased to 194 cm^2/V-s at 373 K (Fig. 5**d**). Similarly, the average weighted mobility of n-BTS 170 μm films was 109 cm^2/V-s at room temperature and decreased to 78 cm^2/V-s at 373 K. Moreover, the high-weighted mobility indicates a higher density of state (DOS) effective mass was achieved for p-BST and n-BTS 170 μm thickness films [47]. It is well known that applying pressure to composite films may induce lattice defects, resulting in a change in DOS effective mass, phonon vibrations, high-weighted mobility, and electrical conductivity [47–49]. XRD and Raman analysis was performed on p-BST and n-BTS powder and 170 μm composite films to confirm the introduction of lattice defects [33,47-51]. XRD peak shifts illustrate changes in d-spacing or lattice spacing, which is determined by Bragg's law, as shown in Eq. (3) [52].

$$d = \frac{n\lambda}{2\sin\theta} \quad (3)$$

where d represents the d-spacing in the lattice, λ is the wavelength of the X-ray, and θ is the diffraction angle (0°-45°) in the XRD pattern. The clear XRD peak shift was observed for p-BST and n-BTS films at (006), (015), and (0015) (**Fig. S3**, Supporting Information), indicating a change in lattice spacing [52]. In addition, the full width at half maxima (FWHM) from Raman spectra of p-BST and n-BTS 170 μm films (Fig. 5**e, f**) indicates the FWHM peak intensity increase and peak shift compared to p-BST and n-BTS powders at all Raman active vibration modes A_{1g}^1, E_g and A_{1g}^2 (62, 108, 160 cm^{-1}) [33,48,49]. The increased FWHM and peak shift suggest that the defects were introduced into the composite films by applied pressure in both n-type and p-type composite films [48,49]. Therefore, the Raman peak shift and increase in FWHM intensity indicate a change of DOS effective mass and increased phonon vibrations due to applied pressure [33,48,49]. The DOS effective mass was calculated using Snyder's Eq. (4) to confirm the change [47].

$$\mu_w \approx \mu\left(\frac{m^*}{m_e}\right)^{\frac{3}{2}} \quad (4)$$

The DOS effective mass for the p-BST and n-type BTS 170 μm films was calculated to be 1.66 and 1.67 m_e respectively using weighted mobility found at 20 MPa, higher than the typical DOS effective mass of 1.1 for BST [47,53]. The reduced weighted mobility of p-BST and n-BTS 170 μm composite films with an increase in temperature aligns with the prediction of deformation potential phonon scattering theory [47].

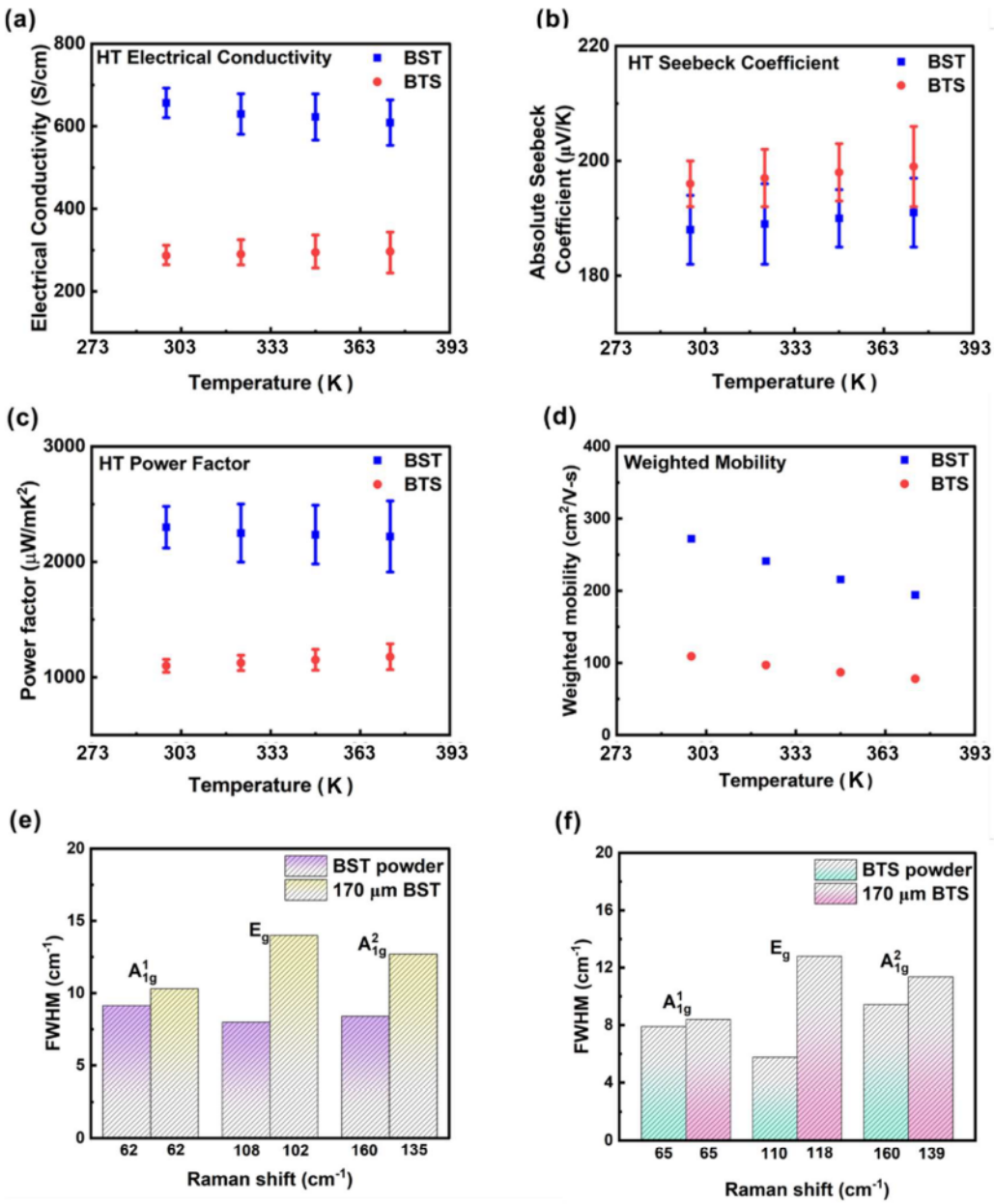

Fig. 5. (a) Electrical conductivity, (b) Absolute Seebeck coefficient, (c) power factor, and (d) weighted mobility of p-BST and n-BTS composite films at different temperatures, (e) FWHM for BST powder and composite 170 μm film, and (f) FWHM for BTS powder and composite 170 μm film confirming peak shift and change of intensity.

3.5. *Thermal conductivity*

In-plane thermal conductivity measurements were performed for 170 and 300 μm thickness films of p-BST and n-BTS to study the effect of low-thermal budget manufacturing method on thermal conductivity. The thermal conductivity for p-BST 170 and 300 μm thickness films was 0.77 and 0.73 W/m-K, respectively, comparable to previously reported binder-based printed composite films [25,28,29,54]. However, this value is less than the thermal conductivity of printed films with the removable binder and bulk BST (0.9-1.5 W/m-K) [18-20,30,39,54]. The lattice thermal conductivity, which mainly depends on phonon transport, for the p-BST 170 μm and 300 μm thickness films was 0.44 and 0.45 W/m-K, respectively. These values were approximately 43% of the BST bulk lattice thermal conductivity (1.04 W/m-K) [39,54,55]. Similarly, the thermal conductivity for n-BTS 170 μm and 300 μm thickness films were 0.65 and 0.64 W/m-K, respectively, comparable to previously reported binder-based printed composite films and lower than bulk BTS (1.6 W/m-K) [14,15,27,42]. Further, the lattice thermal conductivity for n-BTS 170 μm and 300 μm thickness films was 0.5 and 0.54 W/m-K, lower than n-BTS bulk lattice thermal conductivity (1.23 W/m-K) [54, 55]. No significant difference was observed in the thermal conductivities of 170 μm and 300 μm thickness films for both p-BST and n-BTS composites.

We hypothesize that the following four factors could effectively increase the phonon scattering, reducing the lattice thermal conductivity of composite films as compared to bulk: (1) the presence of insulating chitosan binder, (2) the existence of grain-grain and grain-polymer interfaces, (3) increased phonon vibrations and scattering caused by pressure-induced lattice defects, and (4) the density and size of nano-sized defects and TE particles [29,39,46]. The HRTEM images show the presence of p-BST, n-BTS, and chitosan binder, as well as the grain-grain and grain-polymer interfaces in p-BST and n-BTS composite

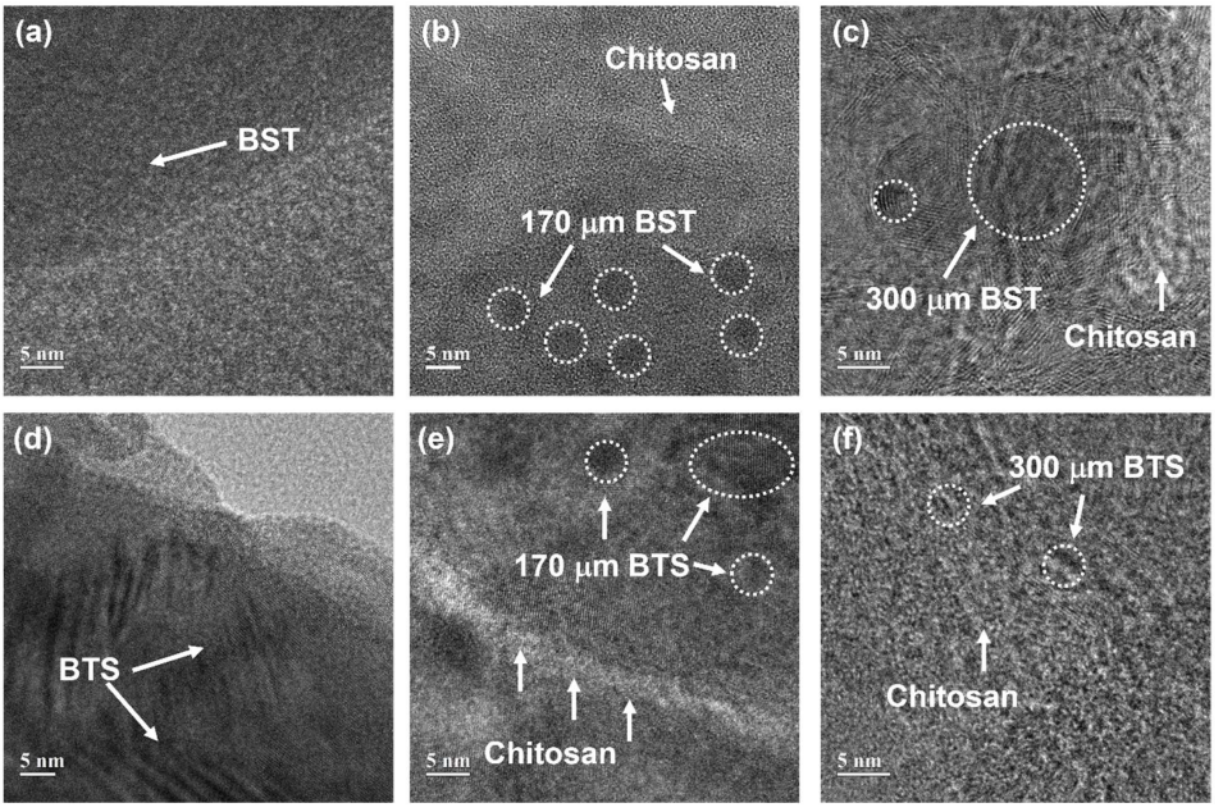

Fig. 6. HRTEM images of (a) BST powder, (b-c) BST 170 μm and 300 μm composite film showing the grains and polymer interfaces, HRTEM images of (d), BTS powder, (e-f) BTS 170 μm and 300 μm composite film showing the TE particles and chitosan interfaces.

films (Fig. 6) [29,41,61-67]. The BST powder shows the presence of only BST particles with no chitosan interface (Fig. 6**a**). The BST 170 and 300 μm composite films show the presence of BST (black particles) and chitosan binder (white region) and grain-binder interfaces (Fig. 6**b,c**). While BTS powder shows the presence of only BTS particles with no chitosan interfaces (Fig. 6**d**), BTS 170 and 300 μm composite films indicate the presence of BTS (black particles), chitosan binder (white region), and grain-binder interfaces (Fig. 6**e,f**). Further, to differentiate the BST and BTS particles, the high-resolution transmission electron microscope (HRTEM) was performed, which clearly depicts the crystalline structure with lattice fringe spacing of BST and BTS particles (**Fig. S4**, Supporting Information). The HRTEM images showed that the lattice spacing increased from 0.215 nm corresponding to (110) crystal plane (BST powder, **Fig. S4a**, Supporting Information) to 0.24 nm corresponding to (1010) crystal plane (BST 170 μm film, **Fig. S4b**, Supporting Information). Similarly, the lattice spacing increased from 0.308 nm (BTS powder, **Fig. S4c**, Supporting Information) to 0.32 nm (BTS 170 μm film, **Fig. S4d**, Supporting Information). The increased lattice spacing corresponds with the defects introduced by applying mechanical pressure [50–51]. In addition, EDAX analysis (**Fig. S5-S10**, Supporting Information) shows the presence of TE particles and chitosan binder (Bi, Sb, Te, C, O, N elements) for p-BST. While the n-BTS 170 and 300 μm composite films show the presence of Bi, Te, Se, C, O, and N elements in the composites [25], the presence of grain-grain and grain-polymer interfaces and insulating chitosan increases the interfacial thermal resistance and lowers the lattice thermal conductivity [25,56-67]. Increased phonon vibrations and scattering caused by pressure-induced lattice defects have been shown by peak shift and change in peak intensity using XRD and Raman (See **Fig. S3**, Fig. 4**e, f**), and the peak shift was confirmed by measuring lattice spacing using HRTEM (**Fig. S4**).

The average nanoparticle and pore size for p-BST and n-BTS 170 and 300 μm composite films was estimated to be ~5 nm using FESEM images and ImageJ software (**Fig. S11** and **S12**, Supporting Information). The total volume occupied by the pores is less than 1% (**Fig. S13** and **S14**, Supporting Information) through Brunauer–Emmett–Teller (BET) analysis. The low volume (~ 1%) occupied by the pores reinforces that these n-type and p-type composite films are dense, as shown earlier. Hellman *et al.* showed that the lattice thermal conductivity of Bi_2Te_3 decreases to less than 0.3 W/m-K when the phonon mean free path is about 10 nm [60]. Lee *et al.* showed that lattice thermal conductivity could be reduced to 0.35W/m-K using a combination of an average grain size of less than 10 nm and a small wt% of nanoparticles and nanopores (~ 0.5 wt%) [58]. However, Dresselhaus *et al.* predicted that charge carriers would pass through without getting scattered when nano features are smaller than 10 nm [56,57]. Based on this work on bulk TE materials, we expect nano-sized TE particles (~ 5 nm), pores (~ 5 nm), and interfaces present in the composite films to only cause phonon scattering [29,39, 46,56,57,60,61]. Therefore, a lower lattice/thermal conductivity was achieved for p-BST and n-BTS 170 and 300 μm thickness films than their bulk values and other binder-free printed composite films without compromising the electrical conductivity. It is worth mentioning that micron-sized TE grains are larger than the electron mean free path, which reduces charge-carrier scattering and contributes to high mobility and electrical conductivity. Therefore, we successfully decoupled electrical and thermal conductivity. The p-BST 170 and 300 μm thickness films have a ZT of 0.89 and 0.81, while the n-BTS 170 and 300 μm thickness films have a ZT of 0.5 and 0.34, respectively, at room temperature. These results confirm that the 170 μm films exhibit a better TE performance than 300 μm thickness films primarily due to higher electrical conductivity. Using interfacial engineering and low-thermal budget printing, we achieved a ZT comparable to the best-reported printed films (**Table S2, S5**, Supporting Information) [19-30,68-71].

3.6. TEG power output characterization

The fabrication of TEG was done using six-couple devices (5 cm × 2

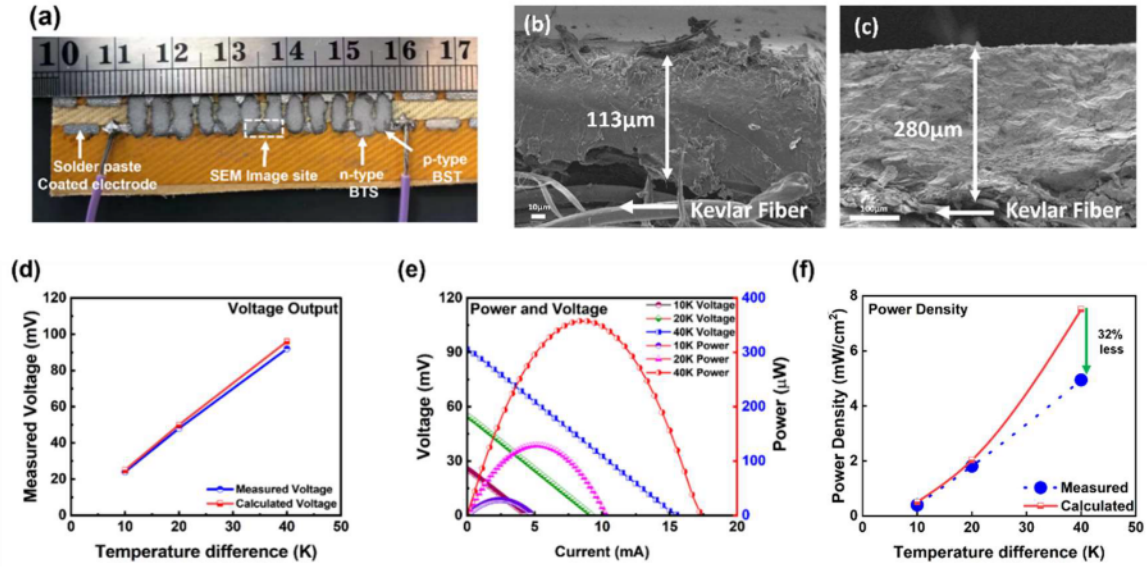

Fig. 7. (a) Photographic image of the fabricated TEG device, (b) cross-sectional SEM image of the solder paste and metal electrode thickness at ends of TEG legs, (c) cross-sectional SEM image of TE material combined with the solder paste and metal electrode at ends of TEG legs, (d) calculated and measured open circuit voltage with respect to temperature difference, (e) TEG voltage, power, and current curve at ΔT of 10, 20, and 40 K, and (f) measured and the calculated ideal power density with respect to temperature difference.

cm × 170 μm) (length × width × height) by a stencil printing method using p-type BST and n-type BTS composite ink. The dimensions of each thermoelectric element leg (TE element) were 7 mm × 3 mm × 170 μm (length × width × height), as shown in Fig. 7**a. Fig. S15** (Supporting Information) shows the custom-built setup for the performance measurement of the TEG. Cross-section SEM images were used to measure the thickness of TE material printed on the TEG device. Fig. 7**b** shows the cross-section SEM with the solder paste and metal electrodes at the ends of the legs within the TEG device, being ~ 113 μm in thickness. Once TE materials were printed, the same area of TEG was ~ 280 μm in thickness (Fig. 7**c**). Therefore, the thickness of the TE element can be confirmed to be ~ 167 μm, similar to the 170 μm film thickness desired. Fig. 7**d,e** shows the voltage and power output characterizations performed at room temperature. The measured voltage output increased linearly with ΔT (Fig. 7**d**) and was comparable to the calculated open-circuit voltage using the Seebeck coefficient of BST and BTS films. The maximum power output of 357.6 μW was achieved at a ΔT of 40 K with a closed circuit voltage of 45.5 mV and a current of 9 mA (Fig. 7**e**). The maximum measured power density of 5.0 mW/cm² (including spacing between thermoelements) was achieved at ΔT of 40 K, shown in Fig. 7**f** [15,16]. The increasing difference between the measured and calculated power density with ΔT can be attributed to the increased device resistance at higher temperatures, confirming the slight decrease in electrical conductivity of the semi-metallic p-BST composite at higher temperatures. The TEG device fabricated using a low-thermal budget method achieved a 45% higher power density than our previous work (**Table S3**, Supporting Information) [25]. It was also comparable to the previous best-reported values of the printed TEG devices (**Table S1**, Supporting Information).

Flexibility and air stability tests were performed to investigate the TEG device durability for practical applications. First, the flexibility test was performed by bending the device at a bending radius of 3 cm for up to 1000 cycles (Fig. 8**a,b**). The device resistance increased by 4.3% only after 1000 cycles of bending, and no measurable change in voltage and 4% change in power at a ΔT of 40 K was observed **(Fig. S16a)** demonstrates its high flexibility and potential application in harvesting waste heat from planar and conformal surfaces.

Next, the stability of the fabricated TEG device was investigated by directly exposing the device to ambient air with no encapsulation for more than six months (Fig. 8**c**). As a result, the device resistance increased by 10% after 48 days and 23% after 184 days with no change in voltage and a 20% decrease in power observed at a ΔT of 40 K showing the oxidization of n-type BTS **(Fig. S16b)**. This indicates the air stability of the fabricated TEG device. Moreover, we powered a blue LED and charged a capacitor to investigate the device's practicality for real-world applications (Fig. 8**d**). Finally, the device was integrated with a voltage step-up circuit (LTC 3108EDE demo board, Linear Technology Corp.), which can amplify the low input voltage (up to 20 mV provided from TEG) to high output voltage (up to 5 V). However, it is worth mentioning that the input voltage realized by the step-up circuit depends on the TEG device internal resistance and voltage output based on Eq. (5).

$$V_L = V_s \frac{R_L}{R_s + R_L} \tag{5}$$

Where V_L is the voltage through the step-up converter, V_s is the voltage provided by the TEG device, R_L is the resistance of the converter, and R_s is the inner resistance of the TEG. The R_L at the input side was measured to be 5.8 Ω by source meter (Keithley 2410-C). The TEG's closed circuit voltage and internal resistance must be sufficient to meet the minimum voltage input requirement of the step-up converter circuit V_L (20 mV).

Three, 4 coupled TEG devices were manufactured with a resistance of 12.6 ohms in total and produced 64 mV of open circuit voltage, sufficient to power the step-up converter at a temperature difference of 17 K (**Fig. S17, S18,** Supporting Information). This integrated TEG was utilized to light up a 2.4 V blue LED at 14 μA (Fig. 8**d**) and charge a capacitor at 25 μA (Fig. 8**e**) [72,73]. Commercially available batteries used in wireless sensors must be periodically charged, interrupting continuous monitoring of physical parameters. Therefore, this work demonstrates that *f*-TEGs integrated with a step-up voltage circuit can charge a capacitor (50 V, 100 μF) and act as a self-sufficient power source for wireless sensor network devices. The charging and discharging voltage of the capacitor was recorded at regular intervals (Fig. 8**e,f**) at a temperature difference of 17 K. It took 6 minutes to charge the capacitor and stabilize its voltage at the 5.1 V outputted by the step-up circuit. The wireless monitoring sensors use less than 10 μW power in sleep mode (~ 96% of time), ~ 300 μW during sensing (~ 4% of time), and ~ 1 mW during communication (~ 0.05% of time) [74,75].

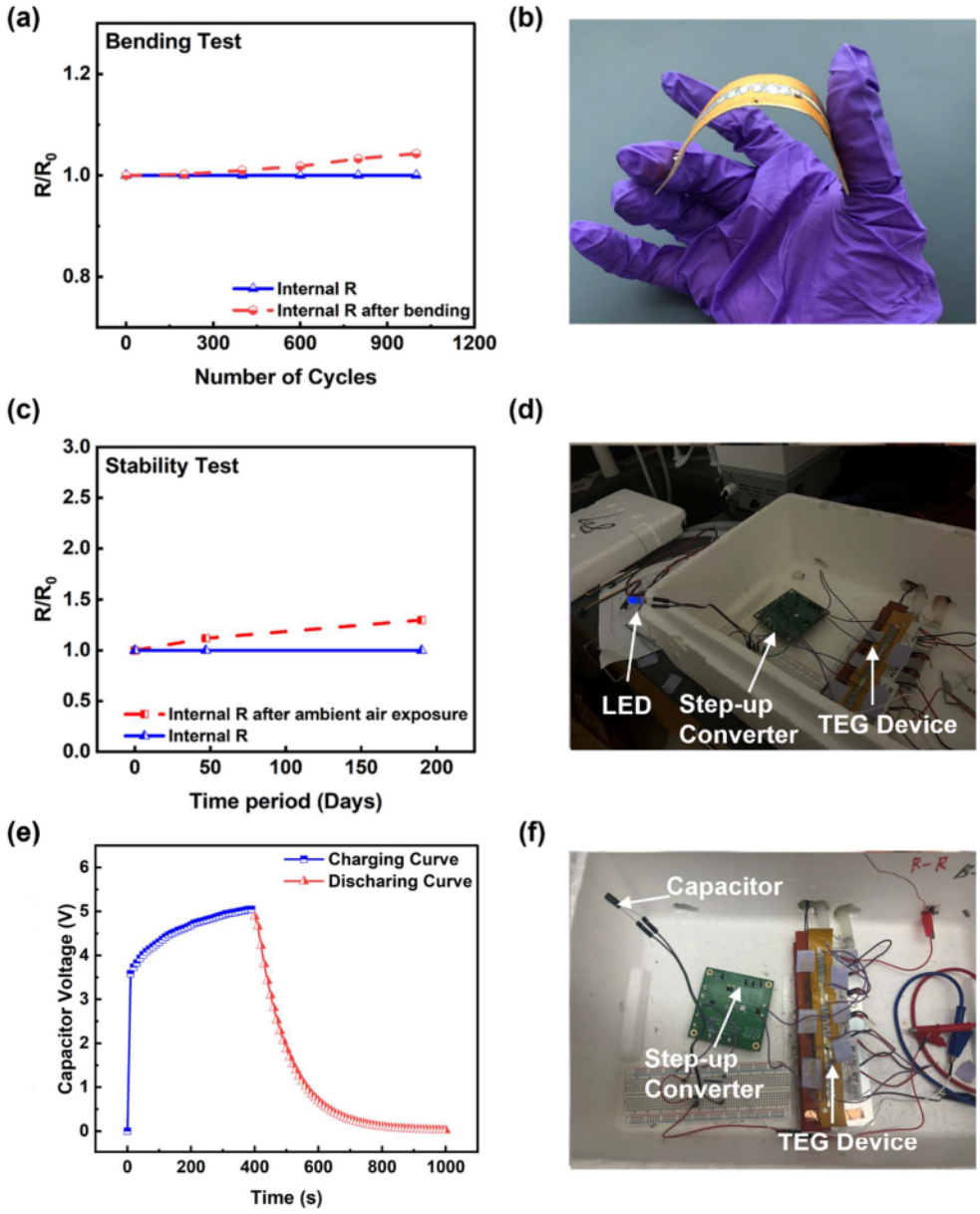

Fig. 8. (a) Normalized resistance of TEG vs. bending cycles, R_0 and R is resistance before and after bending, (b) bending demonstration, (c) normalized resistance of TEG *vs.* exposing time, R_0 and R is resistance before and after exposure to ambient air, (d) LED lighting setup, (e) capacitor voltage with respect to time during charging and discharging, and (f) capacitor charging and discharging setup.

Therefore, the achieved power output of TEG is sufficient for sleep mode, which will be utilized 96% of the time. Hence, integrating TEGs, step-up circuits, and capacitors can meet wireless sensor devices' continuous power requirements and act as self-sufficient power supplies.

In our future works, we will utilize the scalability of our low-cost and energy-efficient manufacturing process to connect a more significant number of TEG devices in series, which can potentially be a self-sufficient and long-lasting power source for many wearable devices to monitor physical parameters continuously using body heat at temperatures differences of 10 K or below [76]. Thus, we believe that the high output voltage obtained could be utilized to charge the capacitors/batteries used in next-generation flexible wireless sensor devices and enable continuous monitoring of physical parameters. The flexibility test, air stability test, LED lighting, and capacitor charging demonstrations confirm the TEG device's capability as a sufficient and long-lasting power supply for multiple wireless sensors and wearable monitoring devices.

4. Conclusion

In summary, this work investigates the synergetic impact of the low-energy input printing method on the micro and nanoscale composite microstructure (grains, grain boundaries, pores, and other defects) and interfaces to decouple the electrical and thermal conductivity. The p-BST-chitosan and n-BTS-chitosan composite films were fabricated using various thicknesses (170, 240, and 300 μm), a small amount of binder (0.05 wt%), heterogenous distribution of micron and nano-sized particles, and applied pressure. The study demonstrates that 170 μm films have fewer micro-scale defects (grains, grain boundaries, grain-chitosan binder interfaces) than 300 μm thickness films. Therefore, the smaller micro-scale defects in 170 μm thickness films caused less charge carrier scattering and higher electrical conductivity. The nanoscale defects introduced by applied pressure, nano-sized TE particles, nanopores, and grain-polymer interface resulted in low thermal conductivity. High electrical conductivity and low thermal conductivity resulted in a ZT of

0.89 for p-BST 170 μm and a ZT of 0.50 for n-BTS 170 μm composite films at room temperature. The higher ZT achieved for p-type and n-type composite films is among the best-reported values for printed films using a low-thermal budget method with a low curing temperature (120°C for 10 min). The achieved power density of 5.0 mW/cm^2 at a temperature difference of 40 K for 6 couple BST-BTS devices stands as a 40% improvement from our previously best reported TEG. Further, the stability and flexibility tests showed that the fabricated TEG device is suitable for practical and real-world applications. Demonstrating LED lighting and capacitor charging at a temperature difference of 17 K confirms the device's capability as a self-sufficient power source for wireless sensor devices. We envisage that the high-performance, flexible, scalable, and air-stable TEG device, fabricated with energy-efficient methods, can be a self-sufficient and long-lasting power source for many wireless sensors to monitor physical parameters continuously.

Supporting Information

Supporting Information is available from the Elsevier Online Library or from the author.

CRediT authorship contribution statement

Jiyuan Huang: Writing – original draft, Methodology, Investigation, Formal analysis, Data curation. **Rohan B. Ambade:** Writing – review & editing, Resources, Data curation. **Jacob Lombardo:** Writing – review & editing, Data curation. **Ben Brooks:** Writing – review & editing, Formal analysis, Data curation. **Aswani Poosapati:** Writing – review & editing, Conceptualization. **Priyanshu Banerjee:** Data curation. **Mortaza Saeidi-Javash:** Investigation, Data curation. **Yanliang Zhang:** Resources, Funding acquisition, Data curation. **Deepa Madan:** Writing – review & editing, Supervision, Resources, Project administration, Funding acquisition, Formal analysis, Conceptualization.

Declaration of competing interest

The authors declare that they have no known competing financial interests or personal relationships that could have appeared to influence the work reported in this paper.

Data availability

Data will be made available on request.

Acknowledgments

The authors thank August Phelps, Abbas Bharmal, Kattab Salih, Kojo Benefo, Salman Mirza, Srushti Kulkarni, Nachammai Nachiappan, and Sakshi Singh for conducting experiments and editing the manuscript. In addition, the authors thank Prof. Erin Lavik for allowing them to use the Keyence microscope. Dr. D. Madan would like to acknowledge the funding support from National Science Foundation under award CMMI-2238996 and TEDCO-Maryland Innovation Initiative. M. S. and Y. Z. would like to acknowledge funding support from the National Science Foundation under award CMMI-1747685. Dr. Rohan would like to acknowledge the funding support from Khalifa University of Science & Technology and Advanced Research & Innovation Center, Aerospace Engineering, Khalifa University of Science & Technology.

Supplementary materials

Supplementary material associated with this article can be found, in the online version, at doi:10.1016/j.apmt.2024.102116.

References

[1] G.J. Snyder, E.S. Toberer, Complex thermoelectric materials, Mater. Sustain. Energy A Collect. Peer Rev. Res. Rev. Artic. Nat. Publ. Gr. 7 (2010) 101–110, https://doi.org/10.1142/9789814317665_0016.
[2] A.F. Ioffe, L.S. Stil'bans, E.K. Iordanishvili, T.S. Stavitskaya, A. Gelbtuch, Semiconductor thermoelements and thermoelectric cooling, Phys. Today 12 (5) (1959) 42, https://doi.org/10.1063/1.3060810.
[3] A. Majumdar, Thermoelectricity in semiconductor nanostructures, Science 303 (5659) (2004) 777–778, https://doi.org/10.1126/science.1093164.
[4] J. Huang, H. Li, E. Kirksey, C. Hoffman, H.J. Jang, J. Wagner, D. Madan, H.E. Katz, Contributions to composite conductivity and Seebeck coefficient in commercial Bi2Te3—Conjugated polymer composites, J. Appl. Phys. 125 (12) (2019) 125502, https://doi.org/10.1063/1.5089872.
[5] E.M.F. Vieira, A.L. Pires, J.P.B. Silva, V.H. Magalhães, J. Grilo, F.P. Brito, M. F. Silva, A.M. Pereira, L.M. Goncalves, High-performance μ-thermoelectric device based on Bi2Te3/Sb2Te3 p–n junctions, ACS Appl. Mater. Interfaces 11 (42) (2019) 38946–38954, https://doi.org/10.1021/acsami.9b13254.
[6] E. Jang, A. Poosapati, D. Madan, Enhanced thermoelectric properties of F4TCNQ doped P3HT and its use as a binder for Sb2Te3 based printed thermoelectric films, ACS Appl. Energy Mater. 1 (4) (2018) 1455–1462, https://doi.org/10.1021/acsaem.7b00231.
[7] H. Lv, L. Liang, Y. Zhang, L. Deng, Z. Chen, Z. Liu, H. Wang, G. Chen, A flexible spring-shaped architecture with optimized thermal design for wearable thermoelectric energy harvesting, Nano Energy 88 (2021) 106260, https://doi.org/10.1016/j.nanoen.2021.106260.
[8] X. Wang, L. Liang, H. Lv, Y. Zhang, G. Chen, Elastic aerogel thermoelectric generator with vertical temperature-difference architecture and compression-induced power enhancement, Nano Energy 90 (2021) 106577, https://doi.org/10.1016/j.nanoen.2021.106577.
[9] L. Liu, J. Chen, L. Liang, L. Deng, G. Chen, A PEDOT:PSS thermoelectric fiber generator, Nano Energy 102 (2022) 107678, https://doi.org/10.1016/j.nanoen.2022.107678.
[10] C. Du, M. Cao, G. Li, Y. Hu, Y. Zhang, L. Liang, Z. Liu, G. Chen, Toward precision recognition of complex hand motions: wearable thermoelectrics by synergistic 2D nanostructure confinement and controlled reduction, Adv. Funct. Mater. 32 (36) (2022) 2206083, https://doi.org/10.1002/adfm.202206083.
[11] G. Li, Y. Hu, J. Chen, L. Liang, Z. Liu, J. Fu, C. Du, G. Chen, Thermoelectric and photoelectric dual modulated sensors for human internet of things application in accurate fire recognition and warning, Adv. Funct. Mater. 33 (2023) 2303861, https://doi.org/10.1002/adfm.202303861.
[12] D. Madan, Z. Wang, P.K. Wright, J.W. Evans, Printed flexible thermoelectric generators for use on low levels of waste heat, Appl. energy 156 (2015) 587–592, https://doi.org/10.1016/j.apenergy.2015.07.066.
[13] D. Madan, Z. Wang, A. Chen, R. Winslow, P.K. Wright, J.W. Evans, Dispenser printed circular thermoelectric devices using Bi and Bi0. 5Sb1. 5Te3, Appl. Phys. Lett. 104 (1) (2014) 013902, https://doi.org/10.1063/1.4861057.
[14] D. Madan, A. Chen, P.K. Wright, J.W. Evans, Printed Se-doped MA n-Type Bi2Te3 thick-film thermoelectric generators, J. Electron. Mater. 41 (2012) 1481–1486, https://doi.org/10.1007/s11664-011-1885-5.
[15] D. Madan, Z. Wang, A. Chen, R.C. Juang, J. Keist, P.K. Wright, J.W. Evans, Enhanced performance of dispenser printed MA n-type Bi2Te3 composite thermoelectric generators, ACS Appl. Mater. Interfaces 4 (11) (2012) 6117–6124, https://doi.org/10.1021/am301759a.
[16] D. Madan, Z. Wang, A. Chen, P.K. Wright, J.W. Evans, High-performance dispenser printed MA p-type Bi0. 5Sb1. 5Te3 flexible thermoelectric generators for powering wireless sensor networks, ACS Appl. Mater. Interfaces 5 (22) (2013) 11872–11876, https://doi.org/10.1021/am403568t.
[17] F. Kim, B. Kwon, Y. Eom, J.E. Lee, S. Park, S. Jo, S.H. Park, B.S. Kim, H.J. Im, M. H. Lee, T.S. Min, K.T. Kim, H.G. Chae, W.P. King, J.S. Son, 3D printing of shape-conformable thermoelectric materials using all-inorganic Bi2Te3-based inks, Nat. Energy 3 (4) (2018) 301–309, https://doi.org/10.1038/s41560-017-0071-2.
[18] T. Varghese, C. Dun, N. Kempf, M. Saeidi-Javash, C. Karthik, J. Richardson, C. Hollar, D. Estrada, Y. Zhang, Flexible thermoelectric devices of ultrahigh power factor by scalable printing and interface engineering, Adv. Funct. Mater. 30 (5) (2020) 1905796, https://doi.org/10.1002/adfm.201905796.
[19] H. Choi, S.J. Kim, Y. Kim, J.H. We, M.W. Oh, B.J. Cho, Enhanced thermoelectric properties of screen-printed Bi0.5Sb1.5Te3 and Bi2Te2.7Se0.3 thick films using a post annealing process with mechanical pressure, J. Mater. Chem. C 5 (33) (2017) 8559–8565, https://doi.org/10.1039/C7TC01797A.
[20] H. Choi, Y.J. Kim, C.S. Kim, H.M. Yang, M.W. Oh, B.J. Cho, Enhancement of reproducibility and reliability in a high-performance flexible thermoelectric generator using screen-printed materials, Nano Energy 46 (2018) 39–44, https://doi.org/10.1016/j.nanoen.2018.01.031.
[21] H. Choi, Y.J. Kim, J. Song, C.S. Kim, G.S. Lee, S. Kim, J. Park, S.H. Yim, S.H. Park, H.R. Hwang, M.H. Hong, P. Veluswamy, B.J. Cho, UV-curable silver electrode for screen-printed thermoelectric generator, Adv. Funct. Mater. 29 (20) (2019) 1901505, https://doi.org/10.1002/adfm.201901505.
[22] X. Yan, W. Zheng, F. Liu, S. Yang, Z. Wang, Thickness effects for thermoelectric property of antimony telluride nanoplatelets via solvothermal method, Sci. Rep. 6 (1) (2016) 1–8, https://doi.org/10.1038/srep37722.
[23] H. Shen, S. Lee, J.G. Kang, T.Y. Eom, H. Lee, S. Han, Thickness dependence of the electrical and thermoelectric properties of co-evaporated Sb2Te3 films, Appl. Surface Sci. 429 (2018) 115–120, https://doi.org/10.1016/j.apsusc.2017.09.037.

[24] N.W. Park, S.I. Park, S.K. Lee, Effect of thickness of single-phase antimony and tellurium thin films on their thermal conductivities, J. Nanosci. Nanotech. 15 (9) (2015) 6729–6733, https://doi.org/10.1166/jnn.2015.11589.

[25] P. Banerjee, J. Huang, R.B. Ambade, E. Jang, M. Saeidi-Javash, Y. Zhang, D. Madan, Effect of particle-size distribution and pressure-induced densification on the microstructure and properties of printable thermoelectric composites and high energy density flexible devices, Nano Energy 89 (2021) 106482, https://doi.org/10.1016/j.nanoen.2021.106482.

[26] E. Jang, A. Poosapati, N. Jang, L. Hu, M. Duffy, M. Zupan, D. Madan, Thermoelectric properties enhancement of p-type composite films using wood-based binder and mechanical pressing, Sci. Rep. 9 (1) (2019) 1–10, https://doi.org/10.1038/s41598-019-44225-z.

[27] P. Banerjee, E. Jang, J. Huang, R. Holley, S. Vadnala, A. Sheikh, A. Trivedi, K. Jackson, V.K. Homman, D. Madan, Thermoelectric performance enhancement of n-type chitosan-Bi2Te2. 7Se0. 3 composite films using heterogeneous grains and mechanical pressure, J. Electron. Mater. 50 (5) (2021) 2840–2851, https://doi.org/10.1007/s11664-021-08798-8.

[28] E. Jang, P. Banerjee, J. Huang, R. Holley, J.T. Gaskins, M.S.B. Hoque, P.E. Hopkins, D. Madan, Thermoelectric performance enhancement of naturally occurring Bi and chitosan composite films using energy efficient method, Electronics (Basel) 9 (3) (2020) 532, https://doi.org/10.3390/electronics9030532.

[29] E. Jang, P. Banerjee, J. Huang, D. Madan, High performance scalable and cost-effective thermoelectric devices fabricated using energy efficient methods and naturally occuring materials, Appl. Energy 294 (2021) 117006, https://doi.org/10.1016/j.apenergy.2021.117006.

[30] S.J. Kim, J.H. We, B.J. Cho, A wearable thermoelectric generator fabricated on a glass fabric, Energy Environ. Sci. 7 (6) (2014) 1959–1965, https://doi.org/10.1039/C4EE00242C.

[31] D. Suh, S. Lee, H. Mun, S.H. Park, K.H. Lee, S.W. Kim, J.Y. Choi, S. Baik, Enhanced thermoelectric performance of Bi0. 5Sb1. 5Te3-expanded graphene composites by simultaneous modulation of electronic and thermal carrier transport, Nano Energy 13 (2015) 67–76, https://doi.org/10.1016/j.nanoen.2015.02.001.

[32] S.W. Ali, S. Rajendran, M. Joshi, Synthesis and characterization of chitosan and silver loaded chitosan nanoparticles for bioactive polyester, Carbohydrate Polym. 83 (2) (2011) 438–446, https://doi.org/10.1016/j.carbpol.2010.08.004.

[33] G. Zheng, X. Su, H. Xie, Y. Shu, T. Liang, X. She, W. Liu, Y. Yan, Q. Zhang, C. Uher, M.G. Kanatzidis, X. Tang, High thermoelectric performance of p-BiSbTe compounds prepared by ultra-fast thermally induced reaction, Energy Environ. Sci. 10 (12) (2017) 2638–2652, https://doi.org/10.1039/C7EE02677C.

[34] D. Han, T. Han, C. Shan, A. Ivaska, L. Niu, Simultaneous determination of ascorbic acid, dopamine and uric acid with chitosan-graphene modified electrode, Electroanalysis 22 (17–18) (2010) 2001–2008, https://doi.org/10.1002/elan.201000094.

[35] D. Li, J.M. Li, J.C. Li, Y.S. Wang, J. Zhang, X.Y. Qin, Y. Cao, Y.S. Li, G.D. Tang, High thermoelectric performance of n-type Bi 2 Te 2.7 Se 0.3 via nanostructure engineering, J. Mater. Chem. A 6 (20) (2018) 9642–9649, https://doi.org/10.1039/C8TA00525G.

[36] Y.S. Wudil, M.A. Gondal, S.G. Rao, S. Kunwar, Thermal conductivity of PLD-grown thermoelectric Bi2Te2. 7Se0. 3 films using temperature-dependent Raman spectroscopy technique, Ceram Int 46 (6) (2020) 7253–7258, https://doi.org/10.1016/j.ceramint.2019.11.219.

[37] Y.Y. Li, X.Y. Qin, D. Li, J. Zhang, C. Li, Y.F. Liu, C.J. Song, H.X. Xin, H.F. Guo, Enhanced thermoelectric performance of Cu2Se/Bi0. 4Sb1. 6Te3 nanocomposites at elevated temperatures, Appl. Phys. Lett. 108 (6) (2016) 062104, https://doi.org/10.1063/1.4941757.

[38] Y. Liu, Y. Zhang, K.H. Lim, M. Ibáñez, S. Ortega, M. Li, J. David, S. Martí-Sánchez, K.M. Ng, J. Arbiol, M.V. Kovalenko, D. Cadavid, A. Cabot, High thermoelectric performance in crystallographically textured n-type Bi2Te3–x sex produced from asymmetric colloidal nanocrystals, ACS Nano 12 (7) (2018) 7174–7184, https://doi.org/10.1021/acsnano.8b03099.

[39] B. Poudel, Q. Hao, Y. Ma, Y. Lan, A. Minnich, B. Yu, X. Yan, D. Wang, A. Muto, D. Vashaee, X. Chen, J. Liu, M.S. Dresselhaus, G. Chen, Z. Ren, High-thermoelectric performance of nanostructured bismuth antimony telluride bulk alloys, Science 320 (5876) (2008) 634–638, https://doi.org/10.1126/science.1156446.

[40] X. Yan, B. Poudel, Y. Ma, W.S. Liu, G. Joshi, H. Wang, Y. Lan, D. Wang, G. Chen, Z. F. Ren, Experimental studies on anisotropic thermoelectric properties and structures of n-type Bi2Te2. 7Se0. 3, Nano Lett. 10 (9) (2010) 3373–3378, https://doi.org/10.1021/nl101156v.

[41] F. Li, X. Huang, Z. Sun, J. Ding, J. Jiang, W. Jiang, L. Chen, Enhanced thermoelectric properties of n-type Bi2Te3-based nanocomposite fabricated by spark plasma sintering, J. Alloy. Compd. 509 (14) (2011) 4769–4773, https://doi.org/10.1016/j.jallcom.2011.01.155.

[42] J.K. Lee, J.H. Son, S.D. Park, S. Park, M.W. Oh, Control of oxygen content of n-type Bi2Te3 based compounds by sintering process and their thermoelectric properties, Mater. Lett. 230 (2018) 211–214, https://doi.org/10.1016/j.matlet.2018.07.119.

[43] L.D. Zhao, B.P. Zhang, W.S. Liu, J.F. Li, Effect of mixed grain sizes on thermoelectric performance of Bi2Te3 compound, J. Appl. Phys. 105 (2) (2009) 023704, https://doi.org/10.1063/1.3063694.

[44] K. Kishimoto, T. Koyanagi, Preparation of sintered degenerate n-type PbTe with a small grain size and its thermoelectric properties, J. Appl. Phys. 92 (5) (2002) 2544–2549, https://doi.org/10.1063/1.1499206.

[45] A. Gharleghi, Y. Liu, M. Zhou, J. He, T.M. Tritt, C.J. Liu, Enhancing the thermoelectric performance of nano-sized CoSb 3 via short-range percolation of electrically conductive WTe 2 inclusions, J. Mater. Chem. A 4 (36) (2016) 13874–13880, https://doi.org/10.1039/C6TA04011J.

[46] S.H. Park, S. Jo, B. Kwon, F. Kim, H.W. Ban, J.E. Lee, D.H. Gu, S.H. Lee, Y. Hwang, J.S. Kim, D.B. Hyun, S. Lee, K.J. Choi, W. Jo, J.S. Son, High-performance shape-engineerable thermoelectric painting, Nat. Commun. 7 (1) (2016) 1–10, https://doi.org/10.1038/ncomms13403.

[47] G.J. Snyder, A.H. Snyder, M. Wood, R. Gurunathan, B.H. Snyder, C. Niu, Weighted mobility, Adv. Mater. 32 (25) (2020) 2001537, https://doi.org/10.1002/adma.202001537.

[48] D.A. Polvani, J.F. Meng, N.V. Chandra Shekar, J. Sharp, J.V. Badding, Large improvement in thermoelectric properties in pressure-tuned p-type Sb1. 5Bi0. 5Te3, Chem. Mater. 13 (6) (2001) 2068–2071, https://doi.org/10.1021/cm000888q.

[49] Z. Wu, X. Chen, E. Mu, Y. Liu, Z. Che, C. Dun, F. Sun, X. Wang, Y. Zhang, Z. Hu, Lattice strain enhances thermoelectric properties in Sb2Te3/Te heterostructure, Adv. Electronic Mater. 6 (1) (2020) 1900735, https://doi.org/10.1002/aelm.201900735.

[50] R. Phillips, K. Jolley, Y. Zhou, R. Smith, Influence of temperature and point defects on the X-ray diffraction pattern of graphite, Carbon Trends 5 (2021) 100124, https://doi.org/10.1016/j.cartre.2021.100124.

[51] C. Zhang, Z. Peng, Z. Li, L. Yu, K.A. Khor, Q. Xiong, Controlled growth of bismuth antimony telluride BixSb2− xTe3 nanoplatelets and their bulk thermoelectric nanocomposites, Nano Energy 15 (2015) 688–696, https://doi.org/10.1016/j.nanoen.2015.05.022.

[52] W.H. Bragg, W.L. Bragg, The reflection of X-rays by crystals, in: Proceedings of the Royal Society of London. Series A, Containing Papers of a Mathematical and Physical Character 88, 1913, pp. 428–438, https://doi.org/10.1098/rspa.1913.0040.

[53] G. Yang, L. Sang, F.F. Yun, D.R.G. Mitchell, G. Casillas, N. Ye, K. See, J. Pei, X. Wang, J. Li, G.J. Snyder, X. Wang, Significant enhancement of thermoelectric figure of merit in BiSbTe-based composites by incorporating carbon microfiber, Adv. Funct. Mater. 31 (15) (2021) 2008851, https://doi.org/10.1002/adfm.202008851.

[54] S. Shin, R. Kumar, J.W. Roh, D.S. Ko, H.S. Kim, S.I. Kim, L. Yin, S.M. Schlossberg, S. Cui, J.M. You, S. Kwon, J. Zheng, J. Wang, R. Chen, High-performance screen-printed thermoelectric films on fabrics, Sci. Rep. 7 (1) (2017) 1–9, https://doi.org/10.1038/s41598-017-01903-0.

[55] H.S. Kim, Z.M. Gibbs, Y. Tang, H. Wang, G.J. Snyder, Characterization of Lorenz number with Seebeck coefficient measurement, APL Mater. 3 (4) (2015) 041506, https://doi.org/10.1063/1.4908244.

[56] A. Minnich, M.S. Dresselhaus, Z.F. Ren, G. Chen, Bulk nanostructured thermoelectric materials: current research and future prospects, Energy Environ. Sci. 2 (5) (2009) 466–479, https://doi.org/10.1039/B822664B.

[57] L.D. Hicks, M.S. Dresselhaus, Thermoelectric figure of merit of a one-dimensional conductor, Phys. Rev. B 47 (24) (1993) 16631, https://doi.org/10.1103/PhysRevB.47.16631.

[58] K.H. Lee, Y.M. Kim, C.O. Park, W.H. Shin, S.W. Kim, H.S. Kim, S.L. Kim, Cumulative defect structures for experimentally attainable low thermal conductivity in thermoelectric (Bi, Sb) 2Te3 alloys, Mater. Today Energy 21 (2021) 100795, https://doi.org/10.1016/j.mtener.2021.100795.

[59] Y.P. Mamunya, V.V. Davydenko, P. Pissis, E.V. Lebedev, Electrical and thermal conductivity of polymers filled with metal powders, Euro. Polym. J. 38 (9) (2002) 1887–1897, https://doi.org/10.1016/S0014-3057(02)00064-2.

[60] O. Hellman, D.A. Broido, Phonon thermal transport in Bi2Te3 from first principles, Phys. Rev. B 90 (13) (2014) 134309, https://doi.org/10.1103/PhysRevB.90.134309.

[61] C.W. Nan, G. Liu, Y. Lin, M. Li, Interface effect on thermal conductivity of carbon nanotube composites, Appl. Phys. Lett. 85 (16) (2004) 3549–3551, https://doi.org/10.1063/1.1808874.

[62] S. Ganguly, C. Zhou, D. Morelli, J. Sakamoto, S.L. Brock, Synthesis and characterization of telluride aerogels: effect of gelation on thermoelectric performance of Bi2Te3 and Bi2–x Sb x Te3 nanostructures, J. Phys. Chem. C 116 (33) (2012) 17431–17439, https://doi.org/10.1021/jp3055608.

[63] D. Portehault, V. Maneeratana, C. Candolfi, N. Oeschler, I. Veremchuk, Y. Grin, C. Sanchez, M. Antonietti, Facile general route toward tunable magnéli nanostructures and their use as thermoelectric metal oxide/carbon nanocomposites, ACS Nano 5 (11) (2011) 9052–9061, https://doi.org/10.1021/nn203265u.

[64] C. Meng, C. Liu, S. Fan, A promising approach to enhanced thermoelectric properties using carbon nanotube networks, Adv. Mater. 22 (4) (2010) 535–539, https://doi.org/10.1002/adma.200902221.

[65] S.I. Kim, K.H. Lee, H.A. Mun, H.S. Kim, S.W. Hwang, J.W. Roh, D.J. Yang, W. H. Shin, X.S. Li, Y.H. Lee, G.J. Snyder, S.W. Kim, Dense dislocation arrays embedded in grain boundaries for high-performance bulk thermoelectrics, Science 348 (6230) (2015) 109–114, https://doi.org/10.1126/science.aaa4166.

[66] C. Jiang, P. Wei, Y. Ding, K. Cai, L. Tong, Q. Gao, Y. Lu, W. Zhao, S. Chen, Ultrahigh performance polyvinylpyrrolidone/Ag2Se composite thermoelectric film for flexible energy harvesting, Nano Energy 80 (2021) 105488, https://doi.org/10.1016/j.nanoen.2020.105488.

[67] S. Sahoo, V.R. Chitturi, R. Agarwal, J.W. Jiang, R.S. Katiyar, Thermal conductivity of free-standing single wall carbon nanotube sheet by Raman spectroscopy, ACS Appl. Mater. Interfaces 6 (22) (2014) 19958–19965, https://doi.org/10.1021/am505484z.

[68] Z. Zheng, X. Shi, D. Ao, W. Liu, M. Li, L. Kou, Y. Chen, F. Li, M. Wei, G. Liang, P. Fan, G. Lu, Z. Chen, Harvesting waste heat with flexible Bi2Te3 thermoelectric thin film, Nat Sustainability 6 (2) (2023) 180–191, https://doi.org/10.1038/s41893-022-01003-6.

[69] D. Ao, W. Liu, Z. Zheng, X. Shi, M. Wei, Y. Zhong, M. Li, G. Liang, P. Fan, Z. Chen, Assembly-free fabrication of high-performance flexible inorganic thin-film thermoelectric device prepared by a thermal diffusion, Adv. Energy Mater. 12 (2022) 2202731, https://doi.org/10.1002/aenm.202202731.

[70] M. Wei, X. Shi, Z. Zheng, F. Li, W. Liu, L. Xiang, Y. Xie, Y. Chen, J. Duan, H. Ma, G. Liang, X. Zhang, P. Fan, Z. Chen, Directional thermal diffusion realizing inorganic Sb2Te3/Te hybrid thin films with high thermoelectric performance and flexibility, Adv. Funct. Mater. 32 (2022) 2207903, https://doi.org/10.1002/adfm.202207903.

[71] D. Ao, W. Liu, Y. Chen, M. Wei, B. Jabar, F. Li, X. Shi, Z. Zheng, G. Liang, X. Zhang, P. Fan, Z. Chen, Novel thermal diffusion temperature engineering leading to high thermoelectric performance in Bi2Te3-based flexible thin-films, Adv. Sci. 9 (2022) 2103547, https://doi.org/10.1002/advs.202103547.

[72] J.P. Ao, H. Sato, T. Mizobuchi, K. Morioka, S. Kawano, Y. Muramoto, Y.B. Lee, D. Sato, Y. Ohno, S. Sakai, Monolithic blue LED series arrays for high-voltage AC operation, Physica status solidi. (a) 194 (2) (2002) 376–379, https://doi.org/10.1002/1521-396X(200212)194:2<376::AID−PSSA376>3.0.CO;2-3.

[73] J. Xu, M. Kong, A. Lin, Y. Song, X. Yu, F. Qu, J. Han, N. Deng, OFDM-based broadband underwater wireless optical communication system using a compact blue LED, Optics Commun 369 (2016) 100–105, https://doi.org/10.1016/j.optcom.2016.02.044.

[74] R. Baldwin, S. Bobovych, R. Robucci, C. Patel, N. Banerjee, Gait analysis for fall prediction using hierarchical textile-based capacitive sensor arrays, in: Design, Automation & Test in Europe Conference & Exhibition, 2015, pp. 1293–1298, https://doi.org/10.7873/DATE.2015.0943.

[75] Y.H. Chee, M. Koplow, M. Mark, N. Pletcher, M. Seeman, F. Burghardt, D. Steingart, J. Rabaey, P. Wright, S. Sanders, PicoCube: a 1cm3 sensor node powered by harvested energy, in: 45th ACM/IEEE Design Automation Conference, 2008, pp. 114–119, https://doi.org/10.1145/1391469.1391499.

[76] A. Tanwar, S. Lal, K.M. Razeeb, Structural design optimization of micro-thermoelectric generator for wearable biomedical devices, Energies 14 (8) (2021) 2339, https://doi.org/10.3390/en14082339.